crystals

MDPI

Article

Development of Additively Manufactured Embedded Ceramic Temperature Sensors via Vat Photopolymerization

Nicholas Reed [1], Rishikesh Srinivasaraghavan Govindarajan [1], Sheridan Perry [2], Kayann Coote [1] and Daewon Kim [1,*]

[1] Department of Aerospace Engineering, Embry-Riddle Aeronautical University, Daytona Beach, FL 32114, USA; reedn4@my.erau.edu (N.R.); srinivr1@erau.edu (R.S.G.); cootek@my.erau.edu (K.C.)
[2] Department of Mechanical Engineering, Embry-Riddle Aeronautical University, Daytona Beach, FL 32114, USA; perrys8@my.erau.edu
* Correspondence: kimd3c@erau.edu

Abstract: Current additive manufacturing (AM) techniques and methods, such as liquid-crystal display (LCD) vat photopolymerization, offer a wide variety of surface-sensing solutions, but customizable internal sensing is both scarce in presence and narrow in scope. In this work, a fabrication process for novel customizable embedded ceramic temperature sensors is investigated. The fabrication techniques and materials are evaluated, followed by extensive characterization via spectral analysis and thermomechanical testing. The findings indicate that LCD-manufactured ceramic sensors exhibit promising sensing properties, including strong linear thermal sensitivity of 0.23% per °C, with an R^2 of at least 0.97, and mechanical strength, with a hardness of 570 HV, making them suitable for adverse environmental conditions. This research not only advances the field of AM for sensor development but also highlights the potential of LCD technology in rapidly producing reliable and efficient ceramic temperature sensors.

Keywords: additive manufacturing; ceramic; high temperature; embedded electrodes; characterization

Citation: Reed, N.; Srinivasaraghavan Govindarajan, R.; Perry, S.; Coote, K.; Kim, D. Development of Additively Manufactured Embedded Ceramic Temperature Sensors via Vat Photopolymerization. *Crystals* **2024**, *14*, 936. https://doi.org/10.3390/cryst14110936

Academic Editor: Jiamin Wu

Received: 20 September 2024
Revised: 24 October 2024
Accepted: 25 October 2024
Published: 29 October 2024

1. Introduction

The design and development of embedded sensing solutions for the structural health monitoring (SHM) of ceramic structures remains challenging due to the spatial and technical requirements for embedded sensors. While ceramic materials are ideal for several high-temperature SHM applications, traditional manufacturing techniques are often unable to effectively produce ceramic substrates conducive to embedded sensing. Specifically, creating and filling complex internal structures into completed and fully solidified structures is often highly ineffective and difficult, if not entirely impossible, for certain substrates with a traditional approach, including ceramics. Additive manufacturing (AM), however, provides a promising solution to the challenges of embedded sensing. Several AM processes, including vat photopolymerization processes, allow the fabrication of complex internal geometries in a desired substrate [1–4]. This process also enables the fabrication of ceramic materials with these complex internal geometries into a solid body, with minimal additional post-processing, enabling the development of embedded ceramic sensors. This work details the development of both surface and fully AM-embedded temperature sensors via vat photopolymerization. It characterizes the materials and processes used and demonstrates effective embedded sensing properties in the final structure by leveraging several advances in AM techniques and materials.

Existing high-temperature sensor solutions have shown that without relying on ceramic shielding or another novel concept, such as aerogel, the maximum survivable temperature for an operational chemical electrode sensor is around 400 °C [5,6]. In contrast, the theoretical upper-temperature limit of metal electrodes and probes is around 800 °C [7,8]. Using a traditional sensor setup without using ceramic shielding or a novel electrode or

substrate material past this temperature becomes increasingly non-viable. Novel sensing components, such as the use of fiber optic cable, have been proven successful with stable response and good sensitivity [9]. Current commercial high-temperature solutions utilize a metal sensor probe that is shielded using materials such as high-purity alumina or silicon carbide as protection [10]. Therefore, it is logical to investigate solutions that use ceramics as a substrate to measure in these extreme environments.

Existing studies show a keen interest in ceramic sensors as an avenue for measuring phenomena in extremely high-temperature environments. One study used yttria–zirconia ceramic as the casing material for an oxygen sensor and found that the sensor remained operable for temperatures up to 700 °C. This study was also able to shield the seal of the internal reference chamber throughout the thermal cycling tests without a significant drop in performance [11]. The use of silicon boron carbonitride (SiBCN) was tested for use as a high-temperature sensing component and was embedded into steel for mechanical strength. This research group found that it could accurately measure temperatures from room temperature to 980 °C [12]. Other studies have utilized alternative materials and found comparable results, such as using silicon aluminum carbonitride (SiAlCN), and found unique properties such as negative temperature coefficient resistance (NTCR) [13]. NTCR is a common property observed in multiple polymer-derived ceramics and has been observed in multiple studies [14]. However, traditional manufacturing of ceramics can be challenging. Since ceramics are difficult to machine with normal manufacturing processes, AM techniques have been used to address these challenges.

Ceramic parts have been manufactured using multiple AM techniques, including vat photopolymerization, material extrusion, and powder bed fusion [15–17]. Studies using vat photopolymerization are of particular interest due to its extremely high precision, which increases the reliability and repeatability in fabrication. In contrast, powder bed fusion requires the melting of a polymer binding agent to generate the green body, leaving a rougher surface finish [18,19]. Material extrusion methods have relatively low accuracy and precision and also tend to produce a poor surface finish [20]. The fabrication of both hard and flexible ceramic sensors has been accomplished using vat photopolymerization [21]. In addition, custom ceramic resin mixtures have been intensely studied in recent years in order to customize the final properties for various use cases [22–24].

Current gaps in research include that most of the ceramic sensors are focused on using polymer-derived ceramic substrates for sensing. Additively manufactured ceramic sensors have been investigated very scarcely, with successful sensors being limited to sapphire fiber optic crystal [25]. Methods such as selective laser sintering (SLS) have been investigated with limited success in embedding sensors. However, due to SLS's inherent limitations, the scope of these studies is highly focused on particular materials, and the surface quality and precision of the final part are much higher than can be produced using other AM methods [26,27]. Other methods have also seen limited success, such as direct ink writing (DIW); however, this success is tempered by the sensor only reading accurately in low temperatures [28]. This paper aims to address these gaps by demonstrating that a sensor can be embedded in a vat photopolymerization-manufactured ceramic outer substrate.

2. Materials and Methods

2.1. Materials and Design

The ceramic material used for the sensor substrate is Vitrolite®, described by the manufacturer as a glass–ceramic UV-curable resin developed by Tethon 3D (Omaha, NE, USA). It is designed for ease of printing in a large portion of commercial 3D vat photopolymerization printers, including desktop printers. Specifically, it requires very low firing temperatures to achieve full densification in the sintering process, reducing the complexity of the equipment necessary to post-process it. The sensor is designed to detect variations in temperature in the sensing layer via resistance change. As the temperature increases, the resistance of a conductive material also varies linearly, which can then be correlated to the temperature change. Silver offers a good temperature coefficient of resistance (α), with pure

silver possessing a coefficient of 0.0038 $^{\circ}C^{-1}$ at 20 °C. Thus, the electrode material used was chosen to be Micromax PE 873, a highly stretchable silver conductive paste developed by DuPont™ (Wilmington, DE, USA). It exhibits excellent conductivity and is easy to work into small sensing channels.

To effectively detect the change in resistance with the change in temperature, a simple electrode patch was designed. Two variants of the sensor electrodes were fabricated, one with surface-embedded electrodes, with the top surface exposed, and one with completely embedded electrodes, with all surfaces encased inside of the ceramic. The channels (a rounded rectangle with 1.5 mm width × 2 mm height) were then filled with the sensing electrode material and wired after curing, as shown in Figure 1.

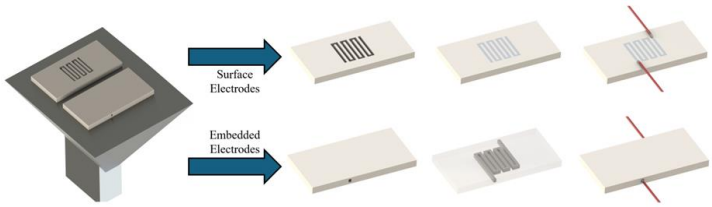

Figure 1. Overall ceramic sensor-fabrication process. The ceramic parts are fabricated utilizing a vat photopolymerization-process. These ceramic substrates are designed and fabricated with either surface-embedded or fully embedded channels. The ceramic parts are then removed from the print base, fully cleaned and post-processed, and sintered. After sintering, the substrates are then filled with silver electrodes and wired to complete the sensor.

2.2. Ceramic Sensor-Manufacturing Process

The main fabrication technique used in the development of the embedded ceramic sensors was the liquid-crystal display (LCD) process. The LCD process is a vat-photopolymerization technique that utilizes a UV light screen to cure individual layers of photosensitive resin material onto a build plate. The build plate then rises as the next layer is cured until an entire model is printed. The LCD process, along with other vat-photopolymerization techniques, enables easy manufacturing of embedded structures.

To fabricate the designed ceramic sensor substrates, a Phrozen Mini 8k LCD printer (Phrozen Technology, Hsinzhu City, Taiwan) was utilized. The Phrozen Mini was chosen due to the very high resolution (22 µm pixel spot size) and relatively large printing volume. Additionally, the Phrozen LCD printer was fitted with an air vat heater, which heated the ceramic resin. This decreased the adhesive force of the material on the nFEP film and reduced the amount of printing failures. The designed ceramic sensors were sliced with Phrozen's proprietary slicing software, Phrozen 3D (version 1092). The printing parameters used for fabrication are listed in Table 1.

Table 1. LCD printer settings.

Parameter	Base Layer	Normal Layer
Exposure Time (s)	80	24
Off Time (s)	10	3
Z Lift (mm)	7	9
Z Lift Speed (mm/min)	25	25
Z Retract Speed (mm/min)	2	10

After printing, the ceramic substrates were rinsed in alternating baths of 99.9% Isopropyl alcohol (IPA) and deionized (DI) water (Duda Diesel, Decatur, AL, USA). The substrates were sonicated while rinsed, and after each rinsing step, compressed air was applied to any internal channels to clear trapped fully liquid or partially cured ceramic resin. After rinsing, the ceramic substrates were dried and cured with a 400 nm 10 W ultraviolet (UV) lamp for 120 s on each side. Finally, any additional printing support material was removed from the substrates, and the parts were sanded at the support connection points to remove sharp protrusions that might affect the sintering of the green body.

2.3. Ceramic Sensor Post-Processing Procedure

Sintering is a critical process in the fabrication of green body ceramics, transforming a compacted powder into a dense, solid material. During sintering, the green body, which is an unsintered ceramic formed by pressing fine powders into a desired shape, is subjected to high temperatures just below its melting point. This heat treatment facilitates atomic diffusion, causing the particles to fuse together, which reduces the size and number of pores. This process enhances the mechanical properties and structural integrity of the ceramic, resulting in a significantly stronger, denser ceramic part. The efficiency and success of sintering are influenced by factors such as temperature, time, and the nature of the ceramic material. Additionally, the LCD process introduces anisotropy into the ceramic green body, which further impacts the efficacy and outcome of the sintering process.

The green body ceramic requires a slow sintering process, which reduces the cracking and warping of the green body as it solidifies. An improved sintering schedule for the LCD printer ceramic green bodies was developed and is shown in Figure 2.

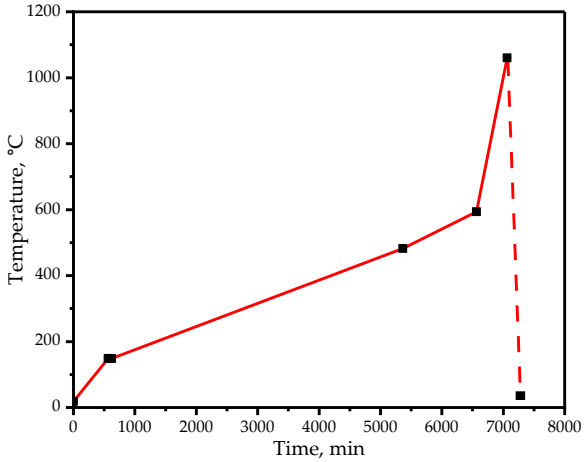

Figure 2. Sintering firing schedule. The sintering process is extended over a long timeframe at a slow heating rate (~0.066 °C per min) in order to reduce cracking and warping. The ceramics are allowed to densify for 10 min at 1060 °C and then are cooled at a rate of 2.5 °C per min.

After the sintering process was completed and the ceramic substrates were allowed to cool, the channels were injected with the PE 873 silver electrode. The part was once again heated to dry the electrode material and then wired to complete the sensor development.

2.4. Raman Spectroscopy

Raman spectroscopy is a useful technique for determining the composition and concentration of crystalline materials, especially in inorganic and nonmetallic structures, including ceramics. When a monochromatic photon source, like a laser, excites a crystalline material, a small amount of inelastically scattered photons causes a shift in energy, which occurs due to a change in vibrational modes of the molecules.

To identify the composition of the green body and sintered ceramic parts, a WiTec Raman probe (Concord, MA, USA) was utilized with a 532 nm excitation wavelength. High-resolution Raman scans utilized an 1800 g/mm grating, a 100× Zeiss (Oberkochen, Baden-Württemberg, Germany) objective, and a 20 mW laser power, while wide-range scans utilized a 600 g/mm grating, a 10× Zeiss objective, and a 10 mW laser power. Regions of interest were identified via microscope and scanned with the peak oscilloscope tool to identify regions of high peak clarity. When possible, 20 accumulations of 1 s exposure were collected and averaged to produce clean Raman peaks without noise.

2.5. Profilometry and X-Ray Imaging

A Keyence VHX-7000 (Itasca, IL, USA) was used to capture high-resolution microscopy images and profilometry data of the green body and sintered ceramic substrates. When

possible, optical enhancements were performed to increase the clarity of the features present in the images. The profilometry scans were taken in a representative 0.5 mm × 0.5 mm square area of the sample identified with microscopy at the maximum resolution.

X-ray micro-computed tomography (micro-CT) SKYSCAN 1275 (Billerica, MA, USA) is a non-destructive imaging technique extensively utilized in a wide variety of scientific fields to examine the internal structure and properties of various structures with high precision. This method employs X-rays to generate detailed cross-sectional images of a specimen, which are subsequently reconstructed into a comprehensive three-dimensional model. In the context of ceramics, micro-CT is particularly valuable for investigating the presence of defects such as cracks, voids, and inclusions. X-ray microtomography scans were taken to examine the completed sensors for any major defects or damage, especially internal defects that were hard to see.

2.6. EDX Spectroscopy

Energy-dispersive X-ray spectroscopy (EDX) is an analytical technique used for the elemental analysis or chemical characterization of a sample. Upon excitation with high-energy X-rays or electrons, the sample emits characteristic X-rays unique to the elements present. These emitted X-rays are subsequently detected and analyzed to ascertain the elemental composition and relative abundance of elements within the sample. The EDX analysis was integrated with scanning electron microscopy (SEM), facilitating precise localization and surface mapping of elemental distributions. High-resolution images of the substrates before and after sintering were captured with a FEI Quanta 650 SEM (Waltham, MA, USA) with a power of 12.5 kV. Additionally, a Bruker XFlash (Billerica, MA, USA) was used to obtain the elemental composition of the materials at the captured areas of interest.

2.7. Electrode Sheet Resistivity

The four-point resistivity-measurement technique is a method employed to determine the electrical resistivity of materials, particularly thin conductive materials. Four equally spaced probes are brought into contact with the center of the surface of a tested material. A known current of 113.5 mA is then introduced through the outer two probes, while the voltage drop is measured across the inner two probes. This approach effectively eliminates contact resistance, which can compromise the accuracy of common two-point resistivity measurements. When correcting for film thickness and size, the data obtained from the four-probe method yield a reliable measure of the material's resistivity and, by extension, conductivity.

The Micromax PE 873 conductive electrode was measured to determine its conductivity and resistivity. PE 873 was placed to a PET film, and a film applicator formed a 50 µm film sheet. This sheet was cut into 50 mm × 50 mm squares, which were tested with an Ossila Four-Point probe (Sheffield, UK) to measure their sheet resistivity.

2.8. Resistance Measurements

After the sensors were fabricated, the resistance values were measured at various temperatures. For the surface temperature sensor (as shown in Figure 1), the ceramic substrate was placed onto a JOANLAB HSC-17T hotplate. The ceramic substrate was allowed to heat up to various temperatures at equilibrium for 30 min, after which a resistance measurement was taken. The temperature of the sensor was measured with a handheld IR thermometer. This thermometer is only effective at determining the surface temperature and does not work well with the internal sensors. To rectify this, the fully embedded sensors were placed into an Accutemp-09 vacuum furnace and were heated to various temperatures. The sensors were allowed to rest at these temperatures for 30 min to ensure even heating throughout the sample at the time of measurement. The sensors were then measured with a Hioki IM3570 LCR meter (Nagano, Japan) to determine the resistance.

2.9. Hardness Testing

Hardness testing is a crucial method used to assess the resistance of ceramic materials to deformation, scratching, and abrasion. Among the different hardness-testing methods, Vickers hardness testing stands out for its ease of measurement and wide testing range, which makes it especially suitable for ceramics. The Vickers method involves pressing a diamond indenter, shaped like a pyramid with a square base and an angle of 136° between opposite faces, into the ceramic under a specified load. The size of the indentation left on the ceramic surface is measured microscopically. The Vickers hardness (HV) is then calculated by dividing the applied load by the surface area of the indentation.

A series of Vicker's tests were performed to measure the hardness of the LCD-printed sintered ceramics. A Wilson Tukon 1202 Micro Hardness tester (Lake Bluff, IL, USA) was used to apply a load to sintered ceramic samples using a Vicker's microindenter. A loading force of 1 kgf was applied at each loading point. The hardness value was derived from the indentation diagonal length according to ASTM C1327-19, with the indent lengths verified with Keyence microscopy and all unacceptable indents removed [29].

3. Results

3.1. Crystalline Spectral Analysis

Figure 3 shows the green body ceramic pieces that showed the correct spectral peaks for the constituent materials of the ceramic resin that can be identified via Raman spectroscopy (calcium oxide does not produce appreciable Raman lines) [30]. Additionally, a large background noise from the resin and other non-crystalline materials, including carbon, was present in the green body scans.

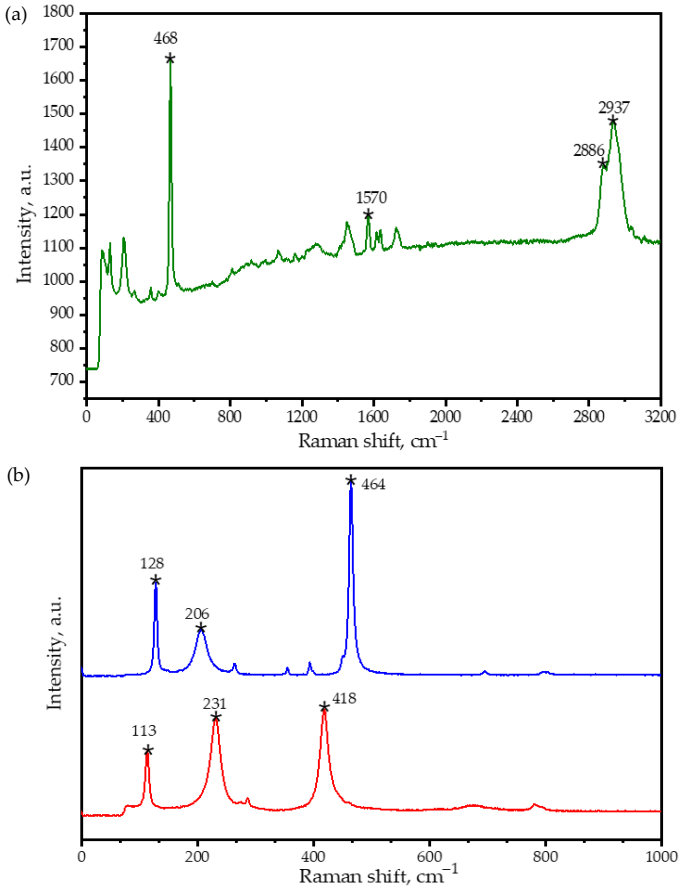

Figure 3. Raman curves for the (**a**) green body ceramic, with distinct characteristic peaks (indicated by *) for silica (468 cm^{-1}), carbon (1570 cm^{-1}), and alumina (2937 cm^{-1}), compared with the (**b**) sintered ceramic peaks, with silica (464, 206, and 128 cm^{-1}) and alumina (418, 231, and 113 cm^{-1}).

After sintering, the two primary constituent materials, aluminum oxide and silicon oxide, were visible in the spectra. As seen in Figure 3, the specific materials are easily identifiable as α-alumina and α-quartz [31–33]. Additionally, the background carbon and other material noise was not present in the sintered scans, indicating that the majority of these materials have burned off. The Raman scans also showed a uniform dispersion of the ceramic materials, even over very tightly controlled regions (~500 µm)

The Raman measurements were able to show the constituent materials of the ceramic resin both green and sintered, correctly identify the phases and distributions of the material with great accuracy and resolution, and spatially track these materials with respect to the embedded sensor inside.

3.2. Surface and Internal Morphological Analysis

The surface profile of the green ceramic body was measured to be relatively smooth, with a low average roughness value (Sa) across the scanned area. The height variations within the 0.5 mm × 0.5 mm square were minimal, confirming the uniformity of the surface. The profile plot, shown in Figure S1, showed a consistent, near-flat line with only minor deviations, which corresponds with the smoothness observed in the microscopy images, as seen in Figure 4.

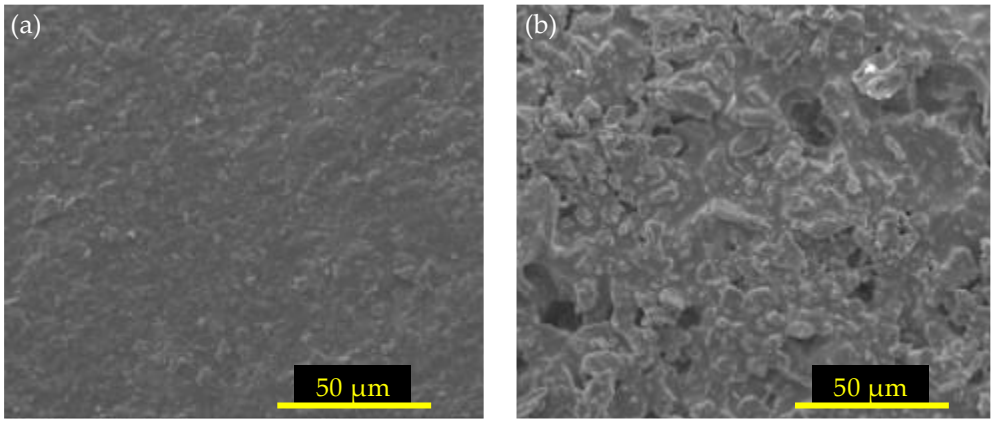

Figure 4. SEM imaging of the (**a**) green body and (**b**) sintered ceramics. The polymer surrounding the ceramic frit is clearly visible in the green body, which then is burned off during sintering, creating a rougher surface.

For the sintered ceramic substrates, the profilometry data indicated a significantly higher surface roughness, as shown in Table 2. The average roughness (Sa) was notably increased, reflecting the more pronounced surface irregularities seen in the microscopy images. The profile plot, as seen in Figure S1, exhibited sharp peaks and valleys corresponding to the visual evidence of a rougher surface texture post-sintering.

Table 2. Measured roughness of the printed green body and sintered parts.

Measurement	Green Body	Sintered
Sa (µm)	1.46	7.31
Sz (µm)	26.16	45.78
Sq (µm)	1.8	9.07
Ssk	0.03	0.07
Sku	3.53	2.53
Sp (µm)	14.5	22.06
Sv (µm)	11.66	20.72

There were no significant defects, such as delamination, large voids, or major cracks, detected in the tomography scans, as shown in Figure 5. The interface between the embedded sensing channel and the ceramic material appeared smooth and continuous, suggesting

a successful embedding process. The internal structure of the embedded sensing electrode itself was also clear, with no visible fractures or internal defects that could compromise its functionality.

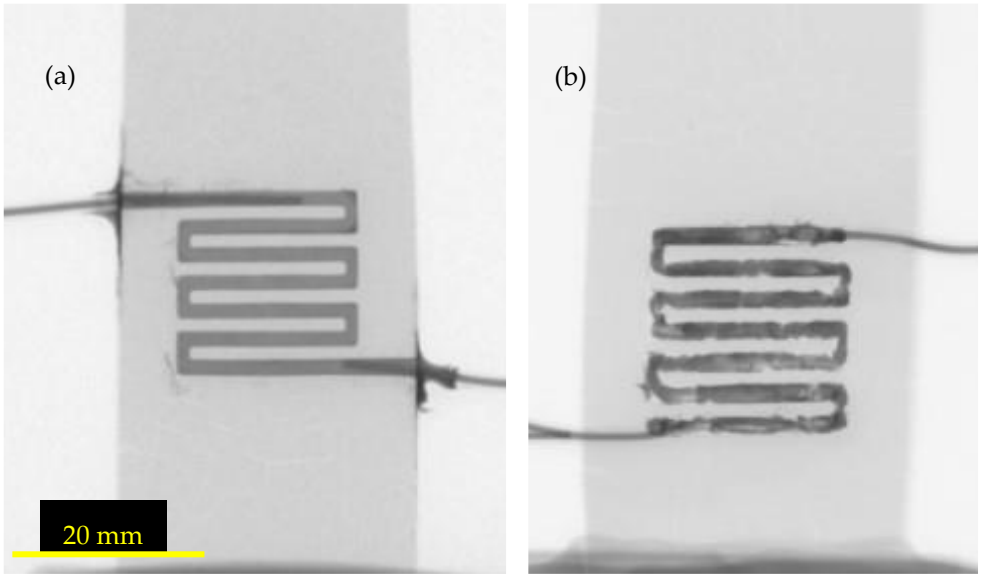

Figure 5. X-Ray microtomography of (**a**) the fully embedded and (**b**) surface-embedded electrode ceramic sensors. The microtomography shows good saturation of the electrode in the channels for effective sensing.

3.3. EDX Analysis

Both the green and sintered ceramic solid parts were measured with EDX analysis to determine the elemental concentration and distribution of the samples. Table 3 shows the results of the EDX analysis showed the following distribution of elements in the sample, which have been additionally compared as relative oxide distributions in Table 4.

Table 3. EDX comparison between green and sintered parts.

Element	Green Norm. Mass (wt. %)	Sintered Norm. Mass (wt. %)
Carbon	49.67	-
Oxygen	39.85	58.22
Silicon	8.12	31.81
Aluminum	2.17	8.21
Calcium	0.19	1.76

Table 4. EDX comparison between green and sintered relative oxide levels.

Element	Green Norm. Oxide Mass (wt. %)	Sintered Norm. Mass (wt. %)	Percent Difference
Silicon	77.48	76.14	1.75
Aluminum	20.71	19.65	5.23
Calcium	1.81	4.21	79.65

The results of the EDX confirmed the prior literature on the composition of the examined ceramic resin, as shown in Figure 6. Furthermore, the resin was free of contamination and impurities.

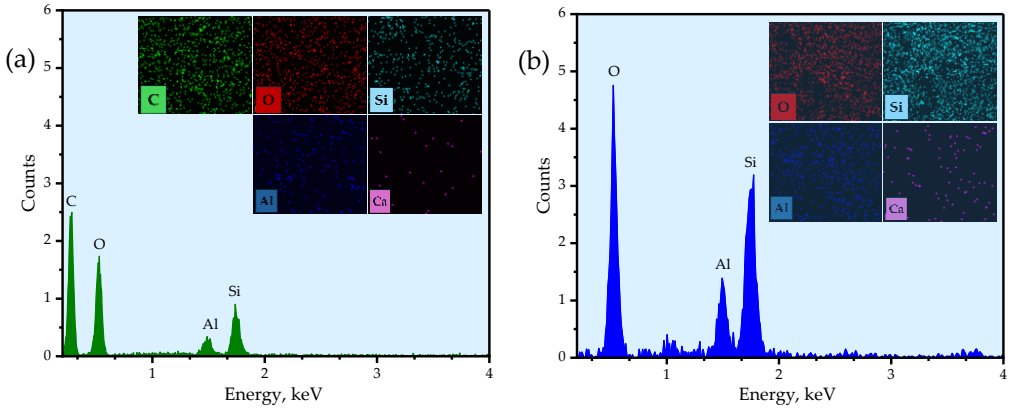

Figure 6. EDX data of the (**a**) green body and the (**b**) sintered ceramic substrates. The green body shows the correct distribution of silica and alumina oxides, with additional carbon-based polymer, while the sintered body shows the removal of the carbon-based elements. The elemental mappings of the EDX scans show an even dispersion of elements throughout the samples.

Additionally, the EDX confirmed an even distribution of the ceramic fillers, without any large agglomerations or sections missing the filler materials. Finally, the removal of carbon in the sintered ceramic EDX confirmed the removal of the polymer material and other additives during the sintering process, leaving only the pure ceramic part.

3.4. Hardness and Electrode Sheet Resistivity Testing

As shown in Table 5, the hardness of the sintered ceramic part was relatively soft, compared to other ceramics, especially compared to the compositional filler materials. The reason for this is twofold. First, with a reduced sintering temperature, the densification of the ceramic is lessened, and the hardness of the ceramics is slightly lower as a result. Secondly, the AM process resulted in a significantly different resulting structure than a traditionally fabricated ceramic, which has been previously shown to reduce hardness [34,35].

Table 5. Hardness and resistivity measurement of sintered ceramic.

Measurement	Density (g/cm^3)	Hardness (HV)	Resistivity (Ω·m)
Mean	2.35	569.77	1.37×10^{-5}
Std. Deviation	0.0783	56.43	1.13×10^{-6}

3.5. The 3D-Printed Ceramic Temperature Sensor Validation

The performance of both the surface embedded sensor and the fully embedded sensor is shown in Figure 7.

For both surface- and fully embedded sensors, with increasing temperature, the resistance was shown to increase linearly. The surface-embedded sensor showed a consistent sensitivity of 0.24% per °C, with a linear increase until the maximum temperature was achieved, with an R^2 of 0.99. Similarly, the fully embedded sensor showed a consistent sensitivity of 0.22% per °C, with an R^2 of 0.98. Both sensors responded rapidly to change in temperature, with very strong linearity throughout the temperature increase.

The embedded sensor, despite the challenging embedded-electrode design, delivered good linear performance under thermal loading. When comparing the results obtained from the embedded sensor to those from surface-embedded sensors, no significant differences were observed, indicating that the embedding process did not compromise sensor accuracy or reliability. Additionally, the sensor demonstrated remarkable stability under thermal conditions; consistent readings were recorded even after the sensor underwent multiple cycles of heating and cooling, with only minimal changes noted.

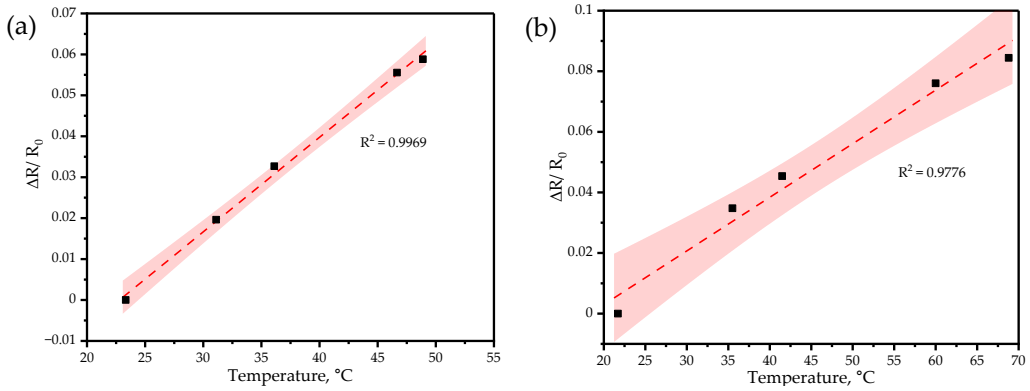

Figure 7. The results of the sensor validation for the (**a**) surface-embedded sensor and (**b**) the fully embedded sensor. Both sensors exhibit strong linear results, with a good thermal resistance response close to that of silver.

4. Conclusions

This work demonstrates an effective set of techniques that can be used to develop and characterize embedded sensors in ceramic substrates. First, the materials used in the design and development of the sensors were analyzed and characterized, to fully model the base sensor material to aid in effective sensor design. Second, both surface- and fully embedded ceramic AM sensors were designed, fabricated, and refined, utilizing vat photopolymerization. Last, the efficacy of the technique was demonstrated with effective temperature sensing, including strong linear sensitivity. The successful integration of sensors within ceramic substrates using vat-photopolymerization processes marks a substantial step forward in AM embedded sensing technology. Future work will seek to characterize more complex sensing materials and substrates in order to further improve sensor performance, especially at higher temperatures. Furthermore, additional work is in progress to address the wiring of the embedded sensors, seeking to create fully wireless=sensing capabilities to further increase the range and scope of embedded sensors. These developments will further increase the durability and lifetime of the embedded sensors, with reduced stress concentrations around the wiring channels. Continued research in embedded sensors in ceramics will likely lead to more advances in SHM for ceramic applications.

Supplementary Materials: The following supporting information can be downloaded at: https://www.mdpi.com/article/10.3390/cryst14110936/s1, Figure S1: Profilometry of the (a) sintered ceramic and (b) green body ceramic. The sintered ceramic shows a marked increase in surface roughness, with sharper peaks and valleys, consistent with the microscopy observations of the ceramic post-sintering.

Author Contributions: Conceptualization, N.R., R.S.G., S.P., K.C. and D.K.; methodology, N.R., R.S.G., S.P. and K.C.; software, N.R. and R.S.G.; validation, N.R. and R.S.G.; formal analysis, N.R. and R.S.G.; investigation, N.R. and R.S.G.; resources, N.R., R.S.G. and D.K.; data curation, N.R.; writing—original draft preparation, N.R., R.S.G. and S.P.; writing—review and editing, N.R., R.S.G., S.P., K.C. and D.K.; visualization, N.R. and R.S.G.; supervision, N.R., R.S.G. and D.K.; project administration, D.K.; funding acquisition, D.K. All authors have read and agreed to the published version of the manuscript.

Funding: This material is based upon work supported by the National Science Foundation under Grant No. 2229155. The opinions, findings, and conclusions or recommendations expressed are those of the author(s) and do not necessarily reflect the views of the National Science Foundation.

Data Availability Statement: The original contributions presented in this study are included in the article/Supplementary Materials. Further inquiries can be directed to the corresponding author.

Conflicts of Interest: The authors declare no conflicts of interest.

References

1. Rehmani, M.A.A.; Jaywant, S.A.; Arif, K.M. Study of Microchannels Fabricated Using Desktop Fused Deposition Modeling Systems. *Micromachines* **2020**, *12*, 14. [CrossRef] [PubMed]
2. Sikulskyi, S.; Srinivasaraghavan Govindarajan, R.; Stark, T.; Ren, Z.; Reed, N.; Kim, D. Two-photon polymerized wetting morphologies for tunable external and internal electrode micropatterning. *Addit. Manuf.* **2024**, *86*, 104220. [CrossRef]
3. Srinivasaraghavan Govindarajan, R.; Ren, Z.; Melendez, I.; Boetcher, S.K.S.; Madiyar, F.; Kim, D. Polymer Nanocomposite Sensors with Improved Piezoelectric Properties through Additive Manufacturing. *Sensors* **2024**, *24*, 2694. [CrossRef] [PubMed]
4. Zhou, Y.; Wu, Y.; Asghar, W.; Ding, J.; Su, X.; Li, S.; Li, F.; Yu, Z.; Shang, J.; Liu, Y.; et al. Asymmetric Structure Based Flexible Strain Sensor for Simultaneous Detection of Various Human Joint Motions. *ACS Appl. Electron. Mater.* **2019**, *1*, 1866–1872. [CrossRef]
5. Cheng, X.; Liu, Y.-T.; Si, Y.; Yu, J.; Ding, B. Direct synthesis of highly stretchable ceramic nanofibrous aerogels via 3D reaction electrospinning. *Nat. Commun.* **2022**, *13*, 2637. [CrossRef]
6. Sui, Y.; Zorman, C.A. Review—Inkjet Printing of Metal Structures for Electrochemical Sensor Applications. *J. Electrochem. Soc.* **2020**, *167*, 037571. [CrossRef]
7. Santra, S.; Guha, P.; Ali, S.; Haneef, I.; Udrea, F. Silicon on Insulator Diode Temperature Sensor—A Detailed Analysis for Ultra-High Temperature Operation. *IEEE Sens. J.* **2010**, *10*, 997–1003. [CrossRef]
8. Zhou, Y.-L.; Cheng, W.-N.; Bai, Y.-Z.; Hou, C.; Li, K.; Huang, Y.-A. Rise of flexible high-temperature electronics. *Rare Met.* **2023**, *42*, 1773–1777. [CrossRef]
9. Gunawardena, D.; Law, O.; Liu, Z.; Zhong, X.; Ho, Y.-T.; Tam, H.-Y. Resurgent regenerated fiber Bragg gratings and thermal annealing techniques for ultra-high temperature sensing beyond 1400 °C. *Opt. Express* **2020**, *28*, 10595. [CrossRef]
10. SOR Controls Group. High Temperature Sensor Assemblies. 2024. Available online: https://www.sorinc.com/products/high-temperature-sensor-assemblies/ (accessed on 8 October 2024).
11. Spirig, J.V.; Ramamoorthy, R.; Akbar, S.A.; Routbort, J.L.; Singh, D.; Dutta, P.K. High temperature zirconia oxygen sensor with sealed metal/metal oxide internal reference. *Sens. Actuators B Chem.* **2007**, *124*, 192–201. [CrossRef]
12. Yan, Q.; Chen, S.; Shi, H.; Wang, X.; Meng, S.; Li, J. Fabrication of polymer-derived SiBCN ceramic temperature sensor with excellent sensing performance. *J. Eur. Ceram. Soc.* **2023**, *43*, 7373–7380. [CrossRef]
13. Shao, P.; Ma, C.; Han, D.; Liu, K.; Li, M.; Liang, Y.; Yao, M.; Wang, H.; Zhang, R.; Shao, G. Temperature-sensing performance of polymer-derived SiAlCN ceramics up to 1000 °C. *Ceram. Int.* **2022**, *48*, 25277–25283. [CrossRef]
14. Yu, Y.; Huang, Q.; Rhodes, S.; Fang, J.; An, L. SiCNO-GO composites with the negative temperature coefficient of resistance for high-temperature sensor applications. *J. Am. Ceram. Soc.* **2017**, *100*, 592–601. [CrossRef]
15. Chen, Z.; Li, Z.; Li, J.; Liu, C.; Lao, C.; Fu, Y.; Liu, C.; Li, Y.; Wang, P.; He, Y. 3D printing of ceramics: A review. *J. Eur. Ceram. Soc.* **2019**, *39*, 661–687. [CrossRef]
16. Dadkhah, M.; Tulliani, J.-M.; Saboori, A.; Iuliano, L. Additive manufacturing of ceramics: Advances, challenges, and outlook. *J. Eur. Ceram. Soc.* **2023**, *43*, 6635–6664. [CrossRef]
17. Prasad, K. Ceramic Sensors: A mini-review of their applications. *Front. Mater.* **2020**, *7*, 593342.
18. Maurya, H.; Kosiba, K.; Juhani, K.; Sergejev, F.; Prashanth, K. Effect of powder bed preheating on the crack formation and microstructure in ceramic matrix composites fabricated by laser powder-bed fusion process. *Addit. Manuf.* **2022**, *58*, 103013. [CrossRef]
19. Wei, C.; Li, L. Recent progress and scientific challenges in multi-material additive manufacturing via laser-based powder bed fusion. *Virtual Phys. Prototyp.* **2021**, *16*, 347–371. [CrossRef]
20. Gonzalez-Gutierrez, J.; Cano, S.; Schuschnigg, S.; Kukla, C.; Sapkota, J.; Holzer, C. Additive Manufacturing of Metallic and Ceramic Components by the Material Extrusion of Highly-Filled Polymers: A Review and Future Perspectives. *Materials* **2018**, *11*, 840. [CrossRef]
21. Zhao, W.; Wang, Z.; Zhang, J.; Wang, X.; Xu, Y.; Ding, N.; Peng, Z. Vat Photopolymerization 3D Printing of Advanced Soft Sensors and Actuators: From Architecture to Function. *Adv. Mater. Technol.* **2021**, *6*, 2001218. [CrossRef]
22. Camargo, I.; Morais, M.; Fortulan, C.; Branciforti, M. A review on the rheological behavior and formulations of ceramic suspensions for vat photopolymerization. *Ceram. Int.* **2021**, *47*, 11906–11921. [CrossRef]
23. Komissarenko, D.; Roland, S.; Seeber, B.; Graule, T.; Blugan, G. DLP 3D printing of high strength semi-translucent zirconia ceramics with relatively low-loaded UV-curable formulations. *Ceram. Int.* **2023**, *49*, 21008–21016. [CrossRef]
24. Komissarenko, D.; Sokolov, P.; Evstigneeva, A.; Shmeleva, I.; Dosovitsky, A. Rheological and Curing Behavior of Acrylate-Based Suspensions for the DLP 3D Printing of Complex Zirconia Parts. *Materials* **2018**, *11*, 2350. [CrossRef] [PubMed]
25. Ghazanfari, A.; Li, W.; Leu, M.; Zhuang, Y.; Huang, J. Advanced ceramic components with embedded sapphire optical fiber sensors for high temperature applications. *Mater. Des.* **2016**, *112*, 197–206. [CrossRef]
26. Petrie, C.; Leonard, D.; Yang, Y.; Trammell, M.; Jolly, B.; Terrani, K. *Embedment of Sensors in Ceramic Structures*; Oak Ridge National Laboratory (ORNL): Oak Ridge, TN, USA, 2019.
27. Petrie, C.; Schrell, A.; Leonard, D.; Jolly, B.; Terrani, K. *Demonstration of Embedded Sensors in Ceramic Structures*; Oak Ridge National Laboratory (ORNL): Oak Ridge, TN, USA, 2020.
28. Marquez, C.; Mata, J.; Renteria, A.; Gonzalez, D.; Gomez, S.; Lopez, A.; Baca, A.; Nuñez, A.; Hassan, M.; Burke, V.; et al. Direct Ink-Write Printing of Ceramic Clay with an Embedded Wireless Temperature and Relative Humidity Sensor. *Sensors* **2023**, *23*, 3352. [CrossRef]

29. *ASTM C1327-19*; Standard Test Method for Vickers Indentation Hardness of Advanced Ceramics. ASTM International: West Conshohocken, PA, USA, 2014. [CrossRef]
30. Schmid, T.; Dariz, P. Shedding light onto the spectra of lime: Raman and luminescence bands of CaO, $Ca(OH)_2$ and $CaCO_3$. *J. Raman Spectrosc.* **2014**, *46*, 141–146. [CrossRef]
31. Cizina, M.F.; Mikesell, T.D.; Kohn, M.J. Optimizing Raman spectral collection for quartz and zircon crystals for elastic thermobarometry. *Am. Mineral. J. Earth Planet. Mater.* **2023**, *108*, 915–927. [CrossRef]
32. Jiang, L.; Liu, Y. Trapiche-like Quartz from Dongwuqi Area, Inner Mongolia, China. *Minerals* **2023**, *13*, 967. [CrossRef]
33. Rebollo-Plata, B.; Sampedro, M.; Gallardo-Gómez, G.; Miranda, N.; Bravo, C.F.; Daniel-Perez, G.; Mateo, B.; Hernández-Cruz, D.; Jiménez-Sandoval, S. Growth of metal micro and/or nanoparticles utilizing arc-discharge immersed in liquid. *Rev. Mex. Fis.* **2014**, *60*, 227–232.
34. Ozer, I.O.; Suvaci, E.; Karademir, B.; Missiaen, J.M.; Carry, C.P.; Bouvard, D. Anisotropic Sintering Shrinkage in Alumina Ceramics Containing Oriented Platelets. *J. Am. Ceram. Soc.* **2006**, *89*, 1972–1976. [CrossRef]
35. Zavaliangos, A.; Missiaen, J.M.; Bouvard, D. Anisotropy in shrinkage during sintering. *Sci. Sinter.* **2006**, *38*, 13–25. [CrossRef]